Significance of ART Algorithm in Acoustic Emission Tomographic Imaging for Damage Visualization in Homogeneous and Multilayer Materials

Md Abdur Rahman

Graduate School of Science and Engineering, Saga University, Saga 840-8502, Japan.

Tawhidul Islam Khan

Faculty of Science and Engineering, Saga University, Saga 840-8502, Japan. E-mail: khan@cc.saga-u.ac.jp

Nazmush Sakib and Tashiro Hibiki

Graduate School of Science and Engineering, Saga University, Saga 840-8502, Japan.

(Received 09 September 2025; accepted 12 January 2026)

This study investigates the application of acoustic emission tomography (AET) using the algebraic reconstruction technique (ART) algorithm for damage detection and visualization in homogeneous and multilayered materials. The research employed a systematic four-stage experimental approach to evaluate how sensor configuration, acoustic signal (ray) coverage, and source signal frequency affect reconstruction accuracy. The first stage examined signal propagation along the surface of a homogeneous aluminum specimen. The second stage analyzed signals propagating through the material volume to provide comprehensive assessment of internal damage. The third stage extended this acoustic emission (AE) tomographic approach to multi-layered structures, revealing additional challenges including impedance mismatches and wave distortions that increased reconstruction errors. The final stage addressed those limitations by implementing higher-frequency source signals, which reduced reconstruction errors and improved damage detection precision due to shorter wavelengths providing finer resolution and greater sensitivity to the defects. The findings demonstrate the effectiveness of AET in identifying damage across diverse material and sensor configurations, ray coverage, and highlight its adaptability as a non-destructive evaluation (NDE) technique. This research provides elaborate and valuable insights into optimizing AET methodologies for structural health monitoring (SHM) and enhancing its applicability to complex material systems using ART algorithm.

1. INTRODUCTION

Acoustic emission tomography (AET) is a non-destructive evaluation (NDE) technique that uses elastic waves generated within stressed materials for structural health monitoring (SHM). When materials experience external forces such as pressure, load, or temperature changes, they produce elastic waves at localized damage sites. These waves propagate through the medium and are detected by receiving sensors. The received signals allow for the identification and visualization of damage at its source.[1] AET plays a vital role in non-destructive testing (NDT), facilitating early detection and visualization of structural irregularities to enhance safety, serviceability, and reduce economic losses.[2,3] This method offers distinct advantages over traditional imaging methods such as X-rays, computed tomography (CT), magnetic resonance imaging (MRI), and ultrasound (UT), which often require intrusive energy sources and cannot capture dynamic material behavior. Instead, AET provides a single-sided, non-intrusive approach by analyzing elastic wave velocity dispersions to visualize the irregularities.[4,5]

This imaging method uses travel-time tomography principles, similar to seismic imaging, where wave arrival times along various ray paths are utilized to reconstruct images by slowness (inverse of velocity) distributions.[2,6] Research in 1970 to 1980s, Rettig and Mansfeld's work on corrosion monitoring and Weng's demonstrations on damage detection in reinforced concrete, established AE as a sensitive tool for identifying structural deterioration. More recently (2012 to 2016), Kobayashi expanded the theoretical and numerical frameworks for 2D and 3D imaging methods of AE tomography.[4,5,7,8] Shiotani's use of AET for crack detection in bridge decks and Aggelis' contributions to damage visualization in concrete, further validating its utility in practical.[9–12] Jiang et al. demonstrated the successful use of the iterative method, in visualizing damage source locations within Q235B steel plates, highlighting its efficacy in structural damage detection.[13]

Tomographic reconstruction techniques fall into two main categories. One category is the transform-based method. It is computationally faster and uses the Fourier theorem. However, it requires scanning the object evenly from all perspectives. Therefore, this method is time-consuming and faces challenges in collecting the necessary AE projection data from critical geometric structures. To overcome these limitations, another category named Iterative technique, which adopts the

algebraic approach, has been proposed. This technique is particularly effective in handling irregular sampling geometries and provides useful results with minimum sensors, minimum rays' coverage, and noisy datasets.[14,15]

Among tomographic reconstruction methods, iterative techniques like ART are particularly well-suited for AET. The ART, derived from Kaczmarz's algorithm, iteratively refines wave slowness distributions by comparing observed and simulated signals.[13,14,16] Initially Gordon, Bender, Herman[17] and Hounsfield[18] proposed that ART delivers high-resolution tomographic images with minimal iterations, balancing computational efficiency and accuracy. However, the application of ART with limited ray projections, single sensor configuration, and source signals frequency impact on tomographic visualization remains unexplored.[12,15,19–21] Thus, the goal of the present research is to address these gaps and visualize the damages in homogenous and multilayered structures by implementing ART method.

The experiments were conducted to validate the effectiveness of the proposed ART method across four experimental stages. In each stage, we increased the number of sensors and ray projections to examine how the reconstruction accuracy improves. In addition, the influence of the source signal frequency was evaluated to understand its role in enhancing damage visualization.

The paper is organized as follows: Section 2 details the theoretical and iterative aspects of the ART. Section 3 describes the experimental methodology, including the experimental setup and signals acquisition in four experimental stages. Section 4 presents the results of four experimental stages, and section 5 provides the conclusion.

2. THEORETICAL ANALYSIS FOR IMAGE RECONSTRUCTION

2.1. Algebraic Reconstruction Technique (ART)

The ART method formulates the image reconstruction challenge as a discrete system. Images are comprised with a discrete two-dimensional array of picture elements called pixels. An image will be built in a one-by-two grid of pixels in Fig. 1. Each pixel is a small square. However, the image that needs to be reconstructed is comprised of an array of unknown pixels, f_j, with $j = 1, 2$. Two linear equations can easily model the set of projections through the pixels. The values of two projections of ray 1 and ray 2 are considered as p_1 and p_2 respectively. The value of a_{ij} is the length (l_{ij}) of the projection ray i that passed through a definite pixel j.

The desired equations from the two projections p_1 and p_2 are given below:

$$a_{11}f_1 + a_{12}f_2 = p_1; \tag{1}$$

$$a_{21}f_1 + a_{22}f_2 = p_2. \tag{2}$$

The generalized equation becomes as:

$$\sum_{j=1}^{N} a_{ij}f_j = p_i; \tag{3}$$

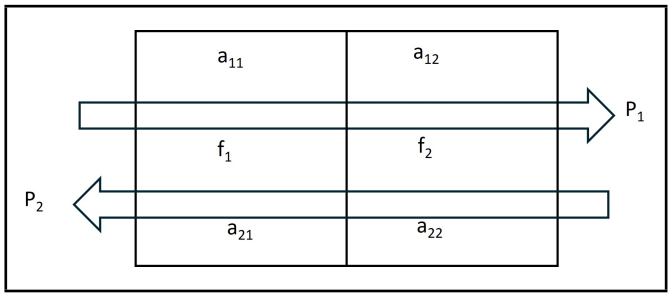

Figure 1. One by two grids of image with two unknown pixels.

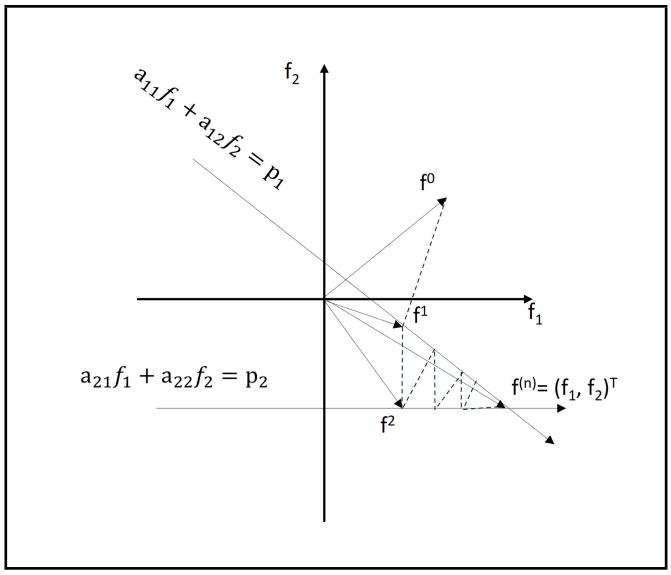

Figure 2. Iterative solution of two straight lines.

where N is the number of the pixels, and $i = \{1, \ldots, M\}$ indicates the index of the projected ray. All projections and unknown pixel values are represented as column vectors, $p = \{p_1, \ldots, p_M\}^T$ and $f = \{f_1, \ldots, f_M\}^T$, respectively. The values of a_{ij} are represented as, $M \times N$ system matrix, such that, the system of equation becomes:

$$P = Af. \tag{4}$$

The system matrix A in Eq. (4) can be designed as below:[22]

$$A = \begin{Bmatrix} a_{11} & a_{12} & \ldots & a_{1N} \\ a_{21} & \ldots & \ldots & a_{2N} \\ \ldots & \ldots & \ldots & \ldots \\ a_{M1} & \ldots & \ldots & a_{MN} \end{Bmatrix}. \tag{5}$$

In Fig. 1, the dimension of the problem is $M = N = 2$, which indicates the desired image consists of two projections within two pixels. The iterative steps for finding two unknown pixel values, f_1 and f_2 can be explained graphically as follows in Fig. 2.

Two straight lines in Fig. 2 represent the system's Eqs. (1) and (2). The meeting point of the two lines gives the solution vector $f = \{f_1, \ldots, f_N\}^T$, i.e., the required pixels of the image. A start of the iteration needs an initial pixel value with an image that is equal to the zero vector, $f^0 = (0, 0, \ldots, 0)^T$, from which the iteration is started. This vector is projected perpendicularly onto the first straight line, representing the first projection beam with the projection result p_1, to obtain a new and enhanced image f^1. Then this image is projected

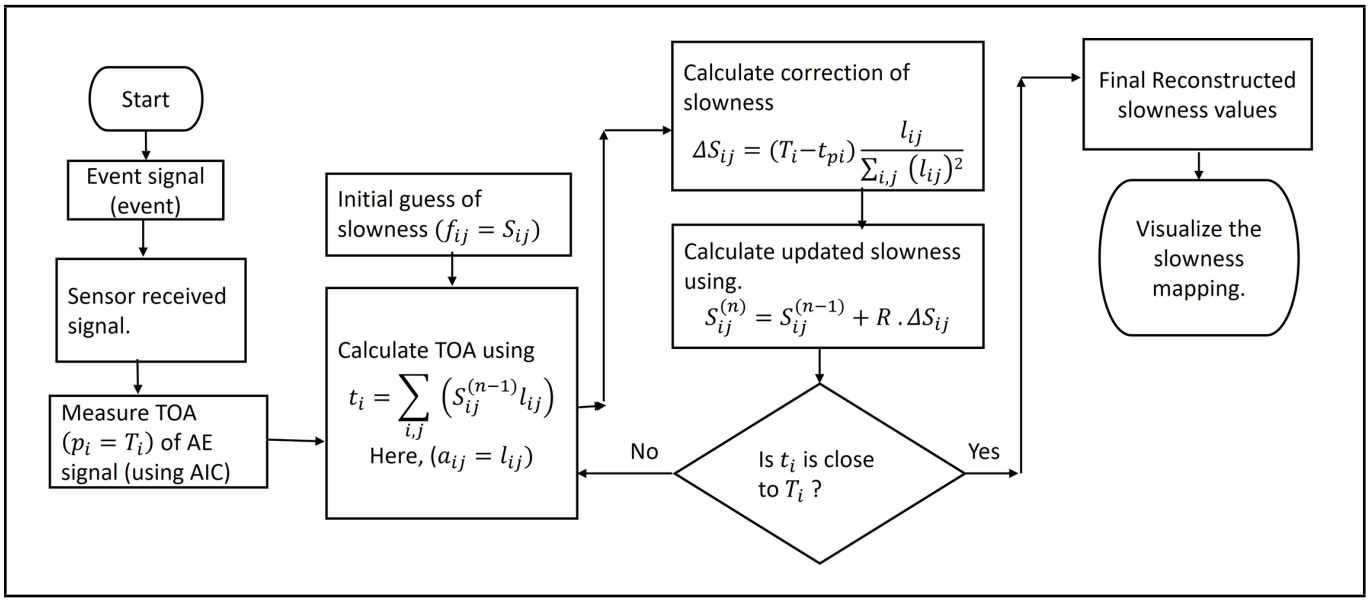

Figure 3. Flow chart of the iteration.

perpendicularly onto the second straight line. In addition, an enhanced image f^2 is received from f^1, because f^2 lies closer to the intersection made by two straight lines (solution point). When taking perpendicular lines gradually from one straight line to another, the distance between two lines reduces. In final iteration step $f^{(n-1)}$ to f^n, the intersection point is reached, which consists of the unknown pixel values of the solution vector. Now, the intersection point, f^n, of the projection lines of Eq. (3) is obtained as follows:

$$a_{i1} f_1 + a_{i2} f_2 = p_i; \tag{6}$$

$$f_2 = -\frac{a_{i1}}{a_{i2}} f_1 + \frac{p_i}{a_{i2}}. \tag{7}$$

Thus, the slope of the line, perpendicular to the projection line is expressed as $\frac{a_{i2}}{a_{i1}}$. Both pixels $(f_1, f_2)^T$, are components of the solution vector f^n. Expressing these pixels (f_1, f_2) in vector form, is consequently true for the relation in Eq. (8). Equation (8) is the final equation for getting the unknown two pixels of the image in Fig. 1:

$$\begin{pmatrix} f_1 \\ f_2 \end{pmatrix} = f^{(n-1)} + \frac{1}{a_i (a_i)^T} \left(p_i - a_i f^{(n-1)}\right) \begin{pmatrix} a_{i1} \\ a_{i2} \end{pmatrix}. \tag{8}$$

Finally, the generalized equation for large numbers of linear equations in AET becomes

$$f^{(n)} = f^{(n-1)} + \frac{(p_i - a_i f^{(n-1)})}{a_i (a_i)^T} (a_i)^T. \tag{9}$$

AET consists of large numbers of equations of projection lines. The unknown pixel values in AET can be obtained from the large number of equations of straight projection lines at different angles and the perpendicular straight lines (broken) in Fig. 2. Therefore, Eq. (9) has been represented for calculating the pixels from the large number of equations in the AET. In Eq. (9), the value of a_i is the system matrix that was built by the length (l_{ij}) of ray i which is passed through a definite pixel j and p_i is the matrix of measured arrival time (T_i) for the projection of the rays. The unknown pixel values represent the slowness in this study.

2.2. Iterative Algorithm

Iterative algorithms are operated by generating successive approximations to converge upon an optimal solution.[23] This algorithm adjusts the slowness of the discrete tomographic cells after each successive iteration. The iteration continues systematically until the computed arrival times, t_i, for a specific projected ray i $(i = 1, \ldots, M)$ match the measured arrival times, T_i. For that reason, the path lengths l_{ij} of each ray i in the tomographic cell and the computed arrival times for iteration $(n-1)$ are used to obtain a new estimate of the slowness of iteration n. These steps depicted in Fig. 3 are performed by passing the ray i through the tomographic cells.

3. EXPERIMENTAL METHODOLOGY

3.1. Experimental Setup

To validate the proposed ART methodology, numerical and experimental investigations were conducted on an aluminum plate with a size of 45 cm in length $\times$ 45 cm in width $\times$ 1.5 cm in thickness. In these investigations, two test configurations were used. One was the Aluminum plate without damage and another one was with a controlled circular damage (containing a 6.2 cm diameter). The damage was introduced to create a geometrical obstacle for signal propagation in the material. A function generator (Model: WF1973) was utilized to generate the AE waves. The excitation signal of the function generator was delivered to the surface of the specimen through an AE transducer (Model: AE-900S-W) (known as event). Two piezoelectric transducers (R15α, and S9208) were used as receiving sensors for collecting generated AE signals from the specimen with a frequency of 150 kHz and 500 kHz respectively. Source frequency of 150 kHz was employed for the first three experimental stages, while 500 kHz was utilized in the fourth experimental stage (details of experimental stages are explained in the next section). The transducers were coupled to the aluminum plate using an acoustic coupling gel (Fig. 4 (b). The receiving sensor was connected to AE signal acquisition system (MISTRASS Express-8, 8 channels) with a preamplifier (models 2/4/6) for signal amplification (gain: 40 dB).

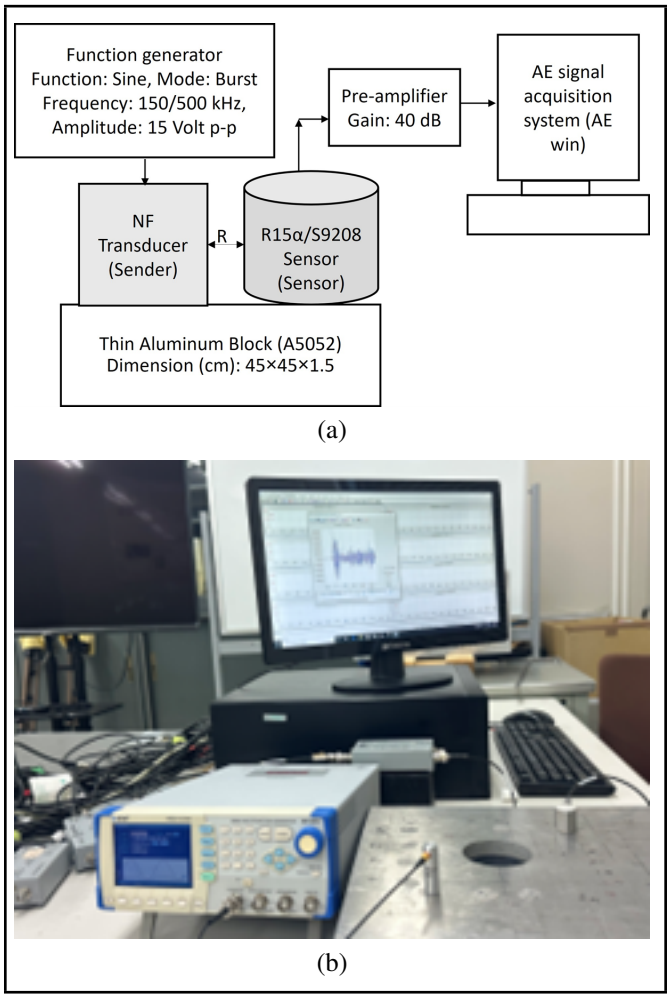

Figure 4. (a) Block diagram of the experiments, and (b) Experimental setup.

The details of the experiment are shown in Figs. 4 (a) and 4 (b).

3.2. Acquisition of Generated AE Signals

The experimental surface was subdivided into an array of cells. The array of cells consists of four-by-four grids comprising 16 unknown pixel values (f_1 to f_{16}) is depicted in Figs. 5 (a) and 5 (b), where R represents the position of receiving sensor (signal receiver) and E represents the position of event source sensor. To address the aims of the research, the experiments were divided into four different experimental stages (procedures).

3.2.1. Experimental Stage 1

In the first stage, the source and the receiver sensors were placed on the same surface of the single layered (homogenous) material. Four experimental cases were conducted in the first stage, to address the challenges of damage visualization with single sensor and limited ray coverage.

Case 1: In this case, the event was conducted at each position of event source, and the projected signal (ray) was received from the corresponding position of the receiver sensor. E_1 represents that event 1 occurred at position 1 and the corresponding signal was received in R_1. Similarly, for eighteen event sources (E_1 to E_{18}), eighteen AE signals were obtained from eighteen receiver positions (R_1 to R_{18}) (Fig. 5 (a)). Each

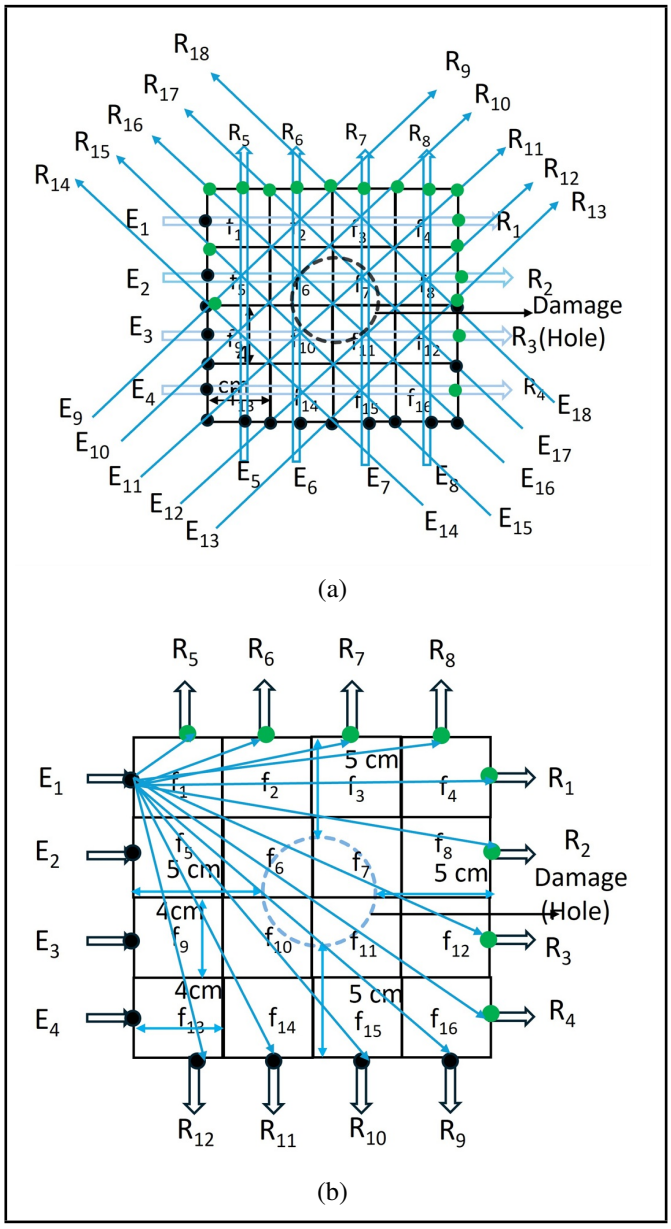

Figure 5. Layout of the experimental surface: (a) Case 1, (b) Case 2.

time, both the event source and receiving source sensors were repositioned to collect the corresponding AE signals.

Case 2: The second case shown in Fig. 5 (b). This case employed a single receiving sensor at twelve different positions (R_1 to R_{12}) for each event of (E_1 to E_4). In Fig. 5 (b), for event 1 ($E1$), twelve rays ($R1$ to $R12$) were collected. Therefore, 48 rays were collected from four events. The ray coverage was improved compared to the previous case. However, the signal acquisition remained constrained using a single sensor.

Case 3: To increase ray coverage and the number of receiving sensors, this case introduced eight receiving sensors (R_1 to R_8) at a time, and eight events (E_1 to E_8) as shown in Fig. 6 (a). For each AE event, signals were received simultaneously from 8 receiver positions. As a result, 64 rays were collected from 8 events (E_1 to E_8) (Fig. 6 (b)).

Case 4: In this case, the positions of the event source and receiver sensors were interchanged mutually with respect to case 3. Therefore, 64 AE signals were collected using the same approach as in case 3. These 64 signals were then combined with the 64 signals of case 3, resulting in a total of 128 signals

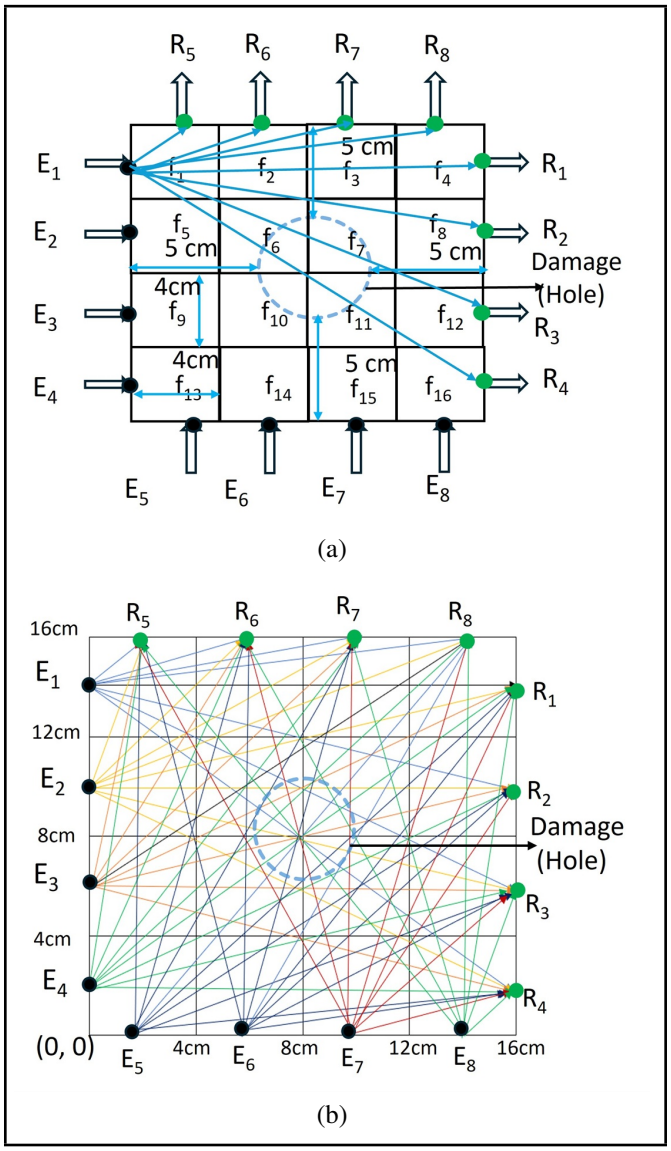

Figure 6. Layout of the: (a) Case 3: AE events and receiver positions, (b) Ray coverage in case 3.

being used for analysis in this case.

In each stage of the experiments, the time of arrival (TOA) of AE signals was calculated for every collected signal using the Akaike information criterion (AIC). The TOA values were then used as input to the ART algorithm, to compute the unknown pixel values.

3.2.2. Experimental Stage 2

In this stage, the AE event source was relocated to the bottom surface of the material and receiving sensors remained on the top (Fig. 7 (a)), for simulating the real-world scenarios with internal or inaccessible damage. This analysis is named AET using the back-surface configuration, where the elastic waves traverse through the material volume. We have used receiving sensors, event sources, and rays' coverage like the case 3 configuration of stage 1. TOA data were collected at eight predefined points on the top surface for each of the eight events on the bottom surface. In Fig. 7 (a), E_0 is the event source sensor, R_n is the receiving sensor, a_n is the distance from AE event source to the signal receiver due to the projection and b_n is the thickness of the material, Δl_{ij} is the length of ray i that passed

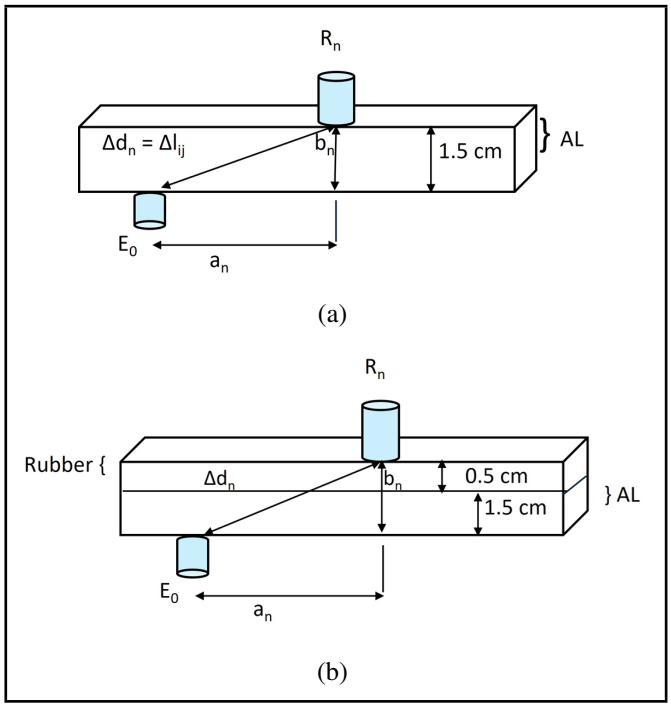

Figure 7. Schematic of the test configuration: (a) Homogenous surface, (b) Multilayer surface.

through a definite pixel j

$$\Delta l_{ij} = \Delta d_n = a_{ij} = \sqrt{a_n^2 + b_n^2}. \tag{10}$$

3.2.3. Experimental Stage 3

In stage 3, we investigated AET in multilayered material, whereas the first two stages focused on experiments conducted on homogeneous surfaces. An aluminum plate covered with a rubber layer was used to evaluate the effectiveness of AET in signal propagation through multiple layers.[24] The AE waves traversed through layered material replicating conditions where internal damage generated through multiple layers. The layout of the multilayer surface is shown in Fig. 7 (b). In the experiment, the AE events were induced on the bottom surface of the aluminum plate, while receiving sensors were positioned on the top of rubber surface, using the case 3 experimental configuration.

3.2.4. Experimental Stage 4

The fourth stage introduced the analysis with high source frequency AE signals (500 kHz) using the back surface configuration. The test was carried out both in homogenous and in multilayered materials.

4. EXPERIMENTAL RESULTS AND DISCUSSION

4.1. Results of Stage 1

The results of 4 experimental cases in stage 1 have been shown in Figs. 8 (a), 8 (b), 8 (c), and 8 (d) respectively. The regions of higher slowness in the figure reflect the presence of the damaged areas. The elastic waves traverse longer and more complex paths, resulting in increased propagation time and slowness in damaged areas. Elevated slowness in surrounding regions arises from redistribution of stress, microstructural

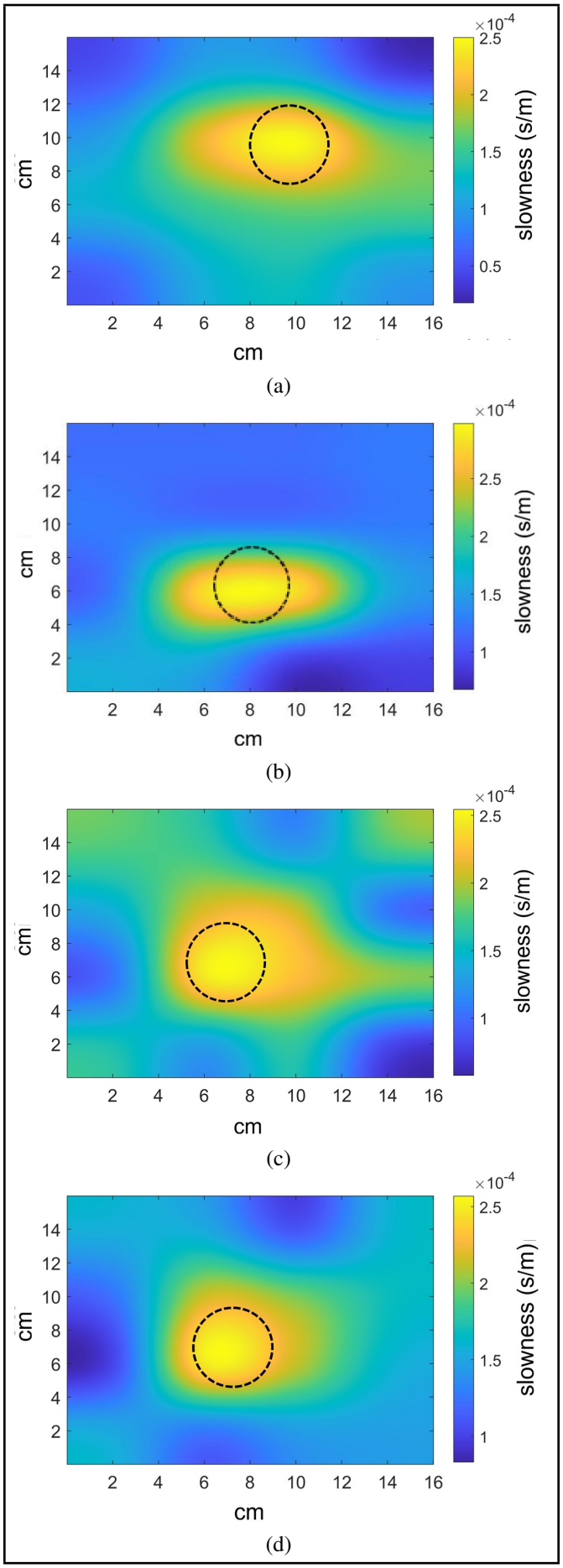

Figure 8. Damage visualization for four cases: (a) Case 1, (b) Case 2, (c) Case 3, (d) Case 4.

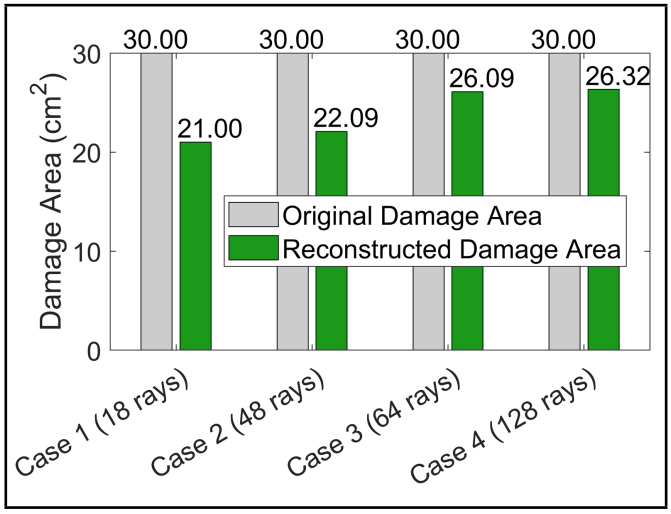

Figure 9. Comparison of the reconstructed damaged area.

adaptation, and wave interactions. The reconstructed damage areas were calculated using the image segmentation method for all four cases by segmenting the higher slowness values. The reconstructed damaged areas and the original damage areas are shown in Fig. 9. Thus, the corresponding errors of the reconstructed areas can be calculated 42.82 %, 35.80 %, 14.70 %, and 13.95 %, respectively for case 1 to 4. Case 1 exhibited the highest error (42.82 %) due to minimal ray coverage and limited spatial resolution. Case 2 improved this error by increasing the ray coverage. Cases 1 and 2 were investigated to detect the damage, where constraints on sensor placement were considered.

Case 3 demonstrated significant improvements in spatial resolution and therefore the error was reduced to 14.70 %. Case 4 represented the most comprehensive configuration in achieving the lowest error rate at 13.95 %, which is 0.75 % error improvement compared to case 3. Both configurations attained superior accuracy through enhanced ray coverage utilizing eight sensors simultaneously, however, case 4 introduced the highest computational complexity and processing time.

Therefore, considering the accuracy and the computational efficiency, case 3 identified as the optimal configuration in this research. Accordingly, this configuration (case 3) was recommended as the baseline for subsequent stages (2, 3 and 4) for AET methodology and to explore its scalability to inaccessible damage regions of homogenous and multilayered materials.

4.2. Results of Stage 2

The result of this stage shows the presence of damage in Fig. 10 (a), indicating the region of higher slowness area. Figure 10 (b) represents the segmented image for damage area calculation. The reconstructed damage area was 24.14 cm^2 as shown in Fig. 10 (c), with an error rate of 19.53 %. The error was caused by more complex wave propagation paths, greater attenuation, and dispersion. These findings validated the algorithm's capability in AET to visualize the damage under challenging conditions. Moreover, the results establish a foundation for extending the method to multilayered materials for enhancing its applicability to heterogeneous structures.

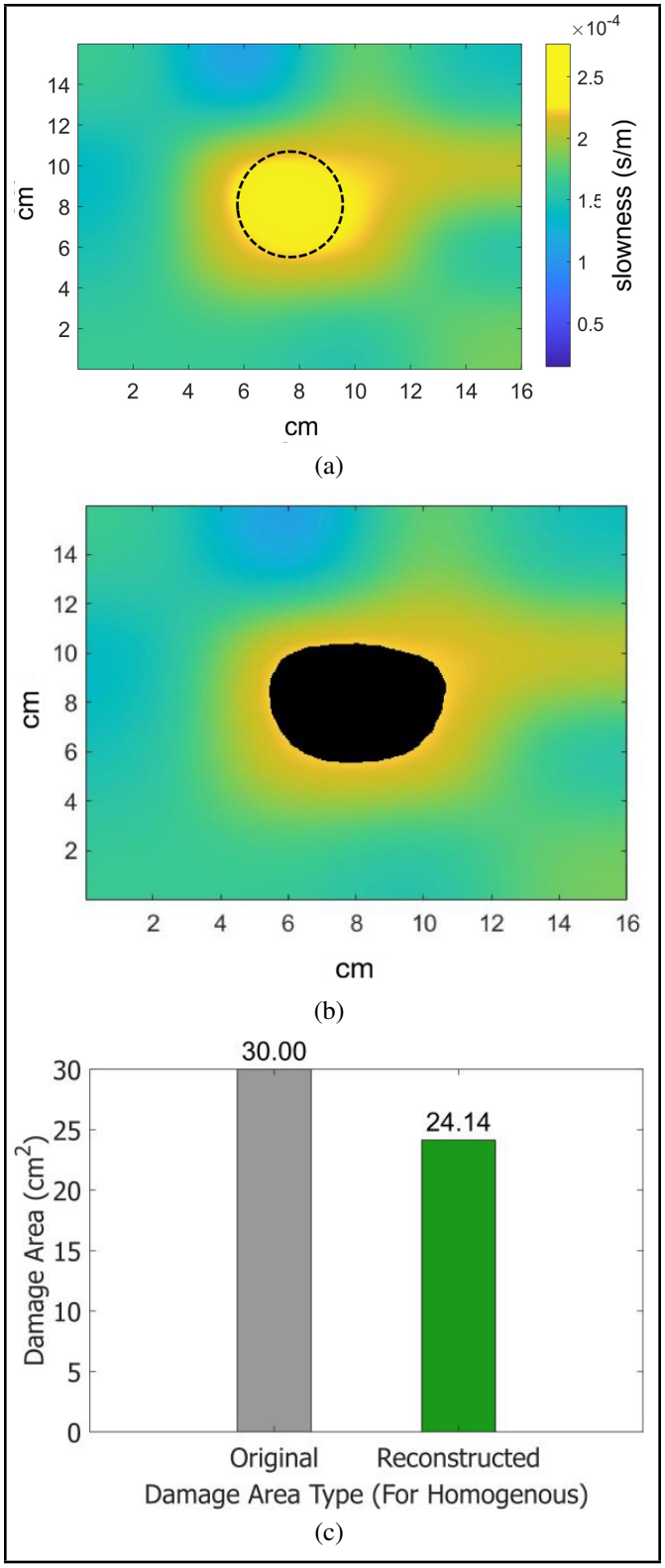

Figure 10. (a) Visualization of damage, (b) Segmented image, (c) Reconstructed damage area.

4.3. Results of Stage 3

The tomographic reconstruction results for multilayered structures are shown in Figs. 11 (a) and 11 (b). The reconstructed damage area was 20.50 cm^2, with an error of 31.47 %, reflecting the challenges of wave propagation in multilayered surface compared to a homogeneous surface. The higher error is attributed to the impedance mismatches at the interfaces between the aluminum and rubber layers, causing wave reflections, refractions, and attenuations. These distortions complicated the propagation paths and slowness distributions. Despite these challenges, the results demonstrate the ability of ART based AET to detect and visualize damage effectively in multilayered material, providing foundation for further refinement. To address these challenges, the next phase of this study focuses on collecting AE signals with higher source frequency to improve damage visualization accuracy.

4.4. Results of Stage 4

In this stage, experiments were conducted both in homogenous and multilayered materials. The results are explained as follows.

Homogenous material: The tomographic visualization of damage in homogenous material for stage 4 is shown in Figs. 12 (a) and 12 (b). The reconstructed damage area for 500 kHz was 25.13 cm^2, as shown in Fig. 12 (c). Thus, the calculated error rate reduced to 16.22 %, compared to 19.53 % using the same configuration with 150 kHz source signals in Stage 2.

Multilayer material: The visualization of damage in the multilayer material is shown in Figs. 13 (a) and 13 (b). The reconstructed damage area was 21.85 cm^2 shown in Fig. 13 (c). The calculated error was reduced to 27.16 %, compared to 31.47 % in the same experiment using a 150 kHz source signal in Stage 3. These results indicate that an improvement is possible by optimizing the collected signals frequency. This frequency optimization attributes to the shorter wavelength for higher resolution with lower wave dispersion of the signal. Thus, the enhanced damage visualization in stage 4 was achieved.

5. CONCLUSIONS

The present research successfully addressed the feasibility of using ART for AE tomographic imaging using a limited number of ray coverages with single sensor configuration. Additionally, the influence of the collected signal frequency was investigated in AET. Damage visualization was achieved using a single sensor with limited AE signals in cases 1 and 2 of stage 1. Although the reconstruction error was higher in these configurations, this research established a foundation for implementing ART-based AET with limited ray coverage and limited sensor placement options in any test object, without any complicated geometry.

In the subsequent stages, both the number of sensors and the coverage of rays were increased. These modifications resulted in improved reconstruction accuracy. However, application to multilayer surfaces led to an increase in reconstruction errors. The increase in errors was effectively mitigated by employing AE signals with higher collected frequency. The progressive enhancement of sensor configuration and optimization

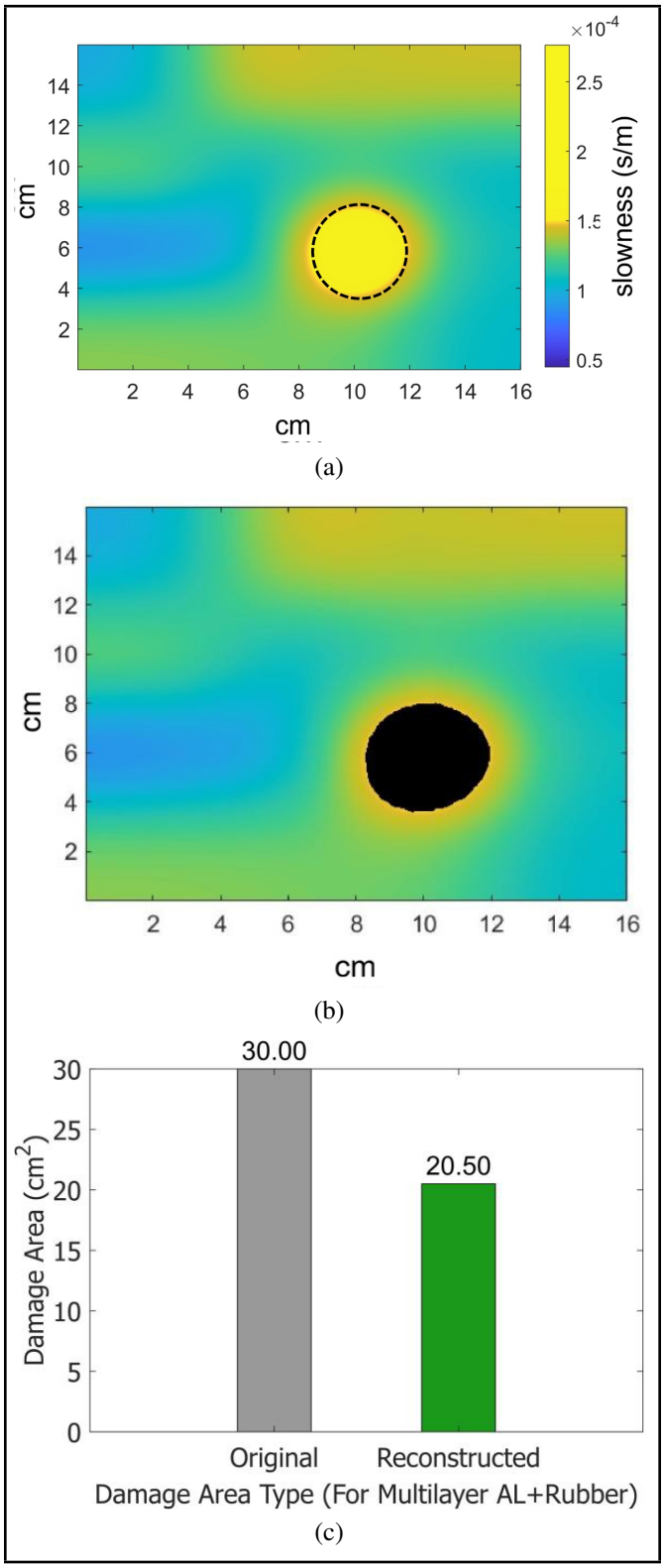

Figure 11. (a) Visualization of damage,(b) Segmented image, (c) Reconstructed damage area.

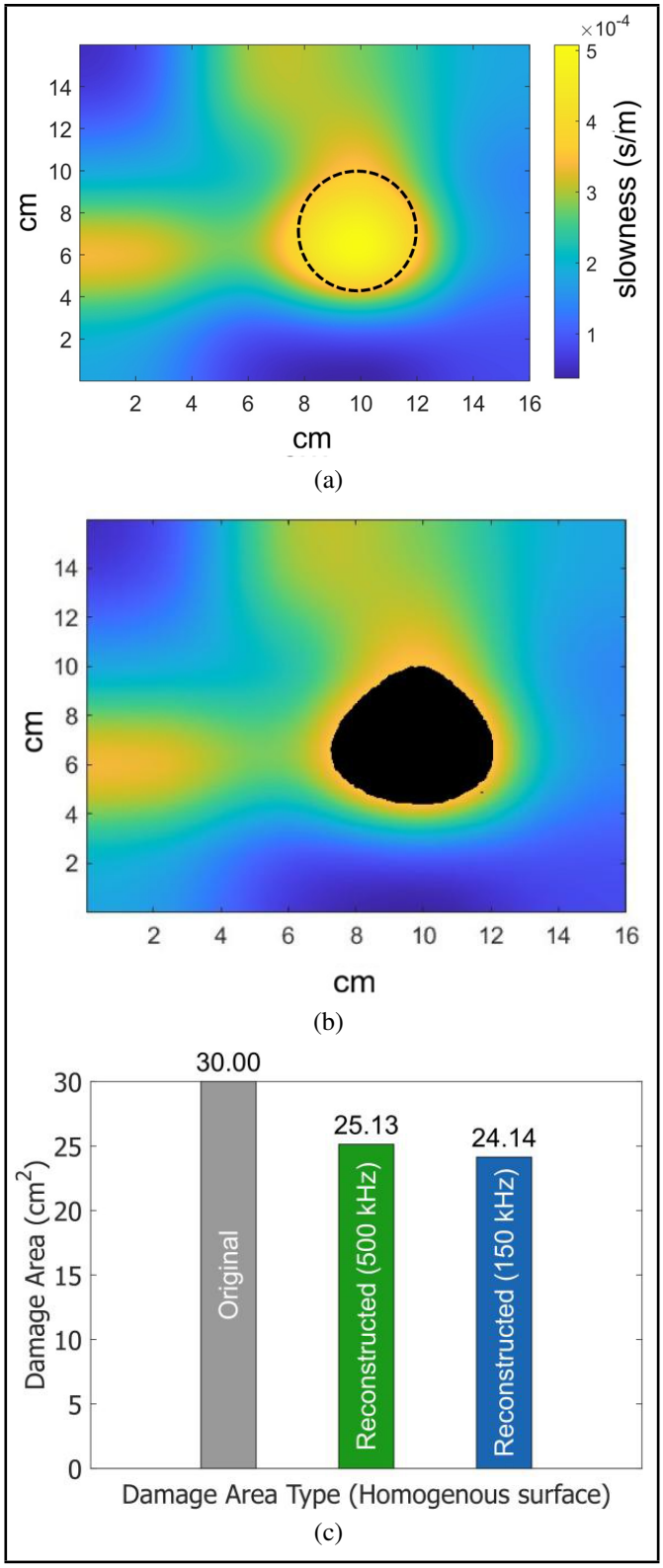

Figure 12. (a) Visualization of damage, (b) Segmented image, (c) Reconstructed damage area.

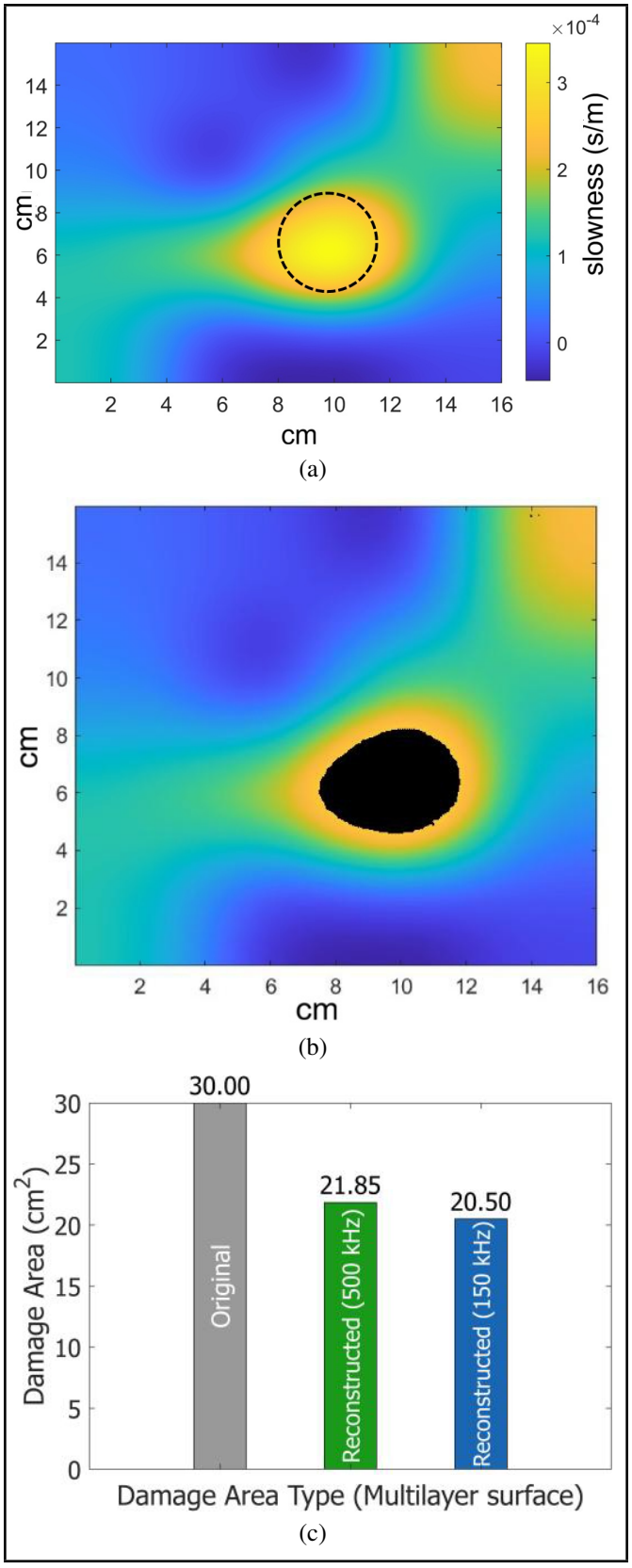

Figure 13. (a) Visualization of damage, (b) Segmented image, (c) Reconstructed damage area.

of signal frequency led to improved accuracy in damage visualization. This provided a versatile baseline for ART-based AET implementation across diverse experimental constraints and testing scenarios.

The validation across different models in this research confirmed the reliability and usefulness of the following key findings:

- **Single-Sensor Detection Capability**: The proposed research demonstrated that damage can be visualized using a single-sensor configuration, indicating the method's applicability to complex geometries with limited sensor placement options.
- **Ray Coverage Optimization**: The first experimental stage demonstrated that single sensors with limited ray coverage successfully detected and visualized damage using the ART algorithm. Subsequent stages revealed that increased ray coverage improved damage reconstruction accuracy; however, this introduced greater computational complexity.
- **Method Robustness**: AE tomography, based on ART effectively identified damage across all proposed configurations, demonstrating its elaborate adaptability for any homogeneous as well as any heterogeneous material.
- **Multilayer Challenges**: The proposed method successfully identified the damage in the complex layered material. Complex structures like layered material increased the reconstruction errors.
- **Source Signal Frequency Effects**: Higher frequencies of the source signals reduced the errors both in homogeneous and layered material. Therefore, optimization in collected signals frequency led to more accurate visualization.

These findings confirm the wide adaptability of AET for damage visualization in diverse material structures, emphasizing the importance of optimizing AE signals, acquisition frequency and sensor configurations with flexible dimensions.

ACKNOWLEDGEMENT

This work has been supported by JSPS KAKENHI Grant Number 21K03948.

REFERENCES

[1] Marihart, H., Lackner, G. and Schauritsch, G. Structural health monitoring using acoustic emission on metallic components in industrial plants, Available at http://www.ndt.net/?id=23605 (accessed March 2026).

[2] Jiang, Y., Xu, F., Xu, B., Jia, M., Hu, J. and Gallego, A. Simulation and experimental investigation on the AE tomography to improve AE source location in the concrete structure, *Mathematical Problems in Engineering*, **2014**, (2014). https://doi.org/10.1155/2014/512406

[3] Liu, L. and Guo, T. Seismic non-destructive testing on a reinforced concrete bridge column using tomographic imaging techniques, *Journal of Geophysics and Engineering*, **2**, 23–31, (2005). https://doi.org/10.1088/1742-2132/2/1/004

[4] Qiao, X., Kobayashi, Y., Oda, K. and Nakamura, K. Improved acoustic emission tomography algorithm based on Lasso regression, *Applied Sciences*, **12**, (2022). https://doi.org/10.3390/app122211800

[5] Maire, E., Carmona, V., Courbon, J. and Ludwig, W. Fast X-ray tomography and acoustic emission study of damage in metals during continuous tensile tests, *Acta Materialia*, **55**, 6806–6815, (2007). https://doi.org/10.1016/j.actamat.2007.08.043

[6] Shah, A. A. and Ribakov, Y. Effectiveness of nonlinear ultrasonic and acoustic emission evaluation of concrete with distributed damages, *Materials and Design*, **31**, 3777–3784, (2010). https://doi.org/10.1016/j.matdes.2010.03.020

[7] Kobayashi, Y. and Shiotani, T. Seismic tomography with estimation of source location for concrete structures, *Proceedings of the Structural Faults and Repair Conference*, Edinburgh, UK, (2012).

[8] Kobayashi, Y., Oda, K. and Shiotani, T. Three-dimensional AE-tomography with accurate source location technique, *Proceedings of the Structural Faults and Repair Conference*, London, UK, (2014).

[9] Chai, H. K., Aggelis, D. G., Momoki, S., Kobayashi, Y. and Shiotani, T. Single-side access tomography for evaluating interior defect of concrete, *Construction and Building Materials*, **24**, 2411–2418, (2010). https://doi.org/10.1016/j.conbuildmat.2010.03.003

[10] Chai, H. K., Momoki, S., Kobayashi, Y., Aggelis, D. G. and Shiotani, T. Tomographic reconstruction for concrete using attenuation of ultrasound, *NDT and E International*, **44**, 206–215, (2011). https://doi.org/10.1016/j.ndteint.2010.11.003

[11] Aggelis, D., Shiotani, T., Momoki, S. and Hirama, A. Acoustic emission and ultrasound for damage characterization of concrete elements, *ACI Materials Journal*, **106**, (2009).

[12] Khan, M. T. I. and Rahman, M. A. Investigating the slowness characteristics in acoustic emission tomography, *INTER-NOISE and NOISE-CON Congress and Conference Proceedings*, **268**, 2367–2371, (2023). https://doi.org/10.3397/IN_2023_0349

[13] Jiang, Y., Xu, F. and Xu, B. Acoustic emission tomography based on simultaneous algebraic reconstruction technique to visualize the damage source location in Q235B steel plate, *Mechanical Systems and Signal Processing*, **64-65**, 452–464, (2015). https://doi.org/10.1016/j.ymssp.2015.04.013

[14] Schubert, F. Basic principles of acoustic emission tomography, *Journal of Acoustic Emission*, **22**, (2004).

[15] Kak, A. C. and Slaney, M. *Principles of computerized tomographic imaging*, (2001). https://doi.org/10.1137/1.9780898719277

[16] Jiang, Y., Xu, F., Gallego, A., Sagata, F. and dos Santos Filho, O. G. Acoustic emission tomography to improve source location in concrete material using SART, *Advances in Acoustic Emission Technology: Proceedings of the World Conference on Acoustic Emission 2013*, 323–335, (2013). https://doi.org/10.1007/978-1-4939-1239-1_30

[17] Gordon, R., Bender, R. and Herman, G. T. Algebraic reconstruction techniques (ART) for three-dimensional electron microscopy and X-ray photography, *Journal of Theoretical Biology*, **29**, (1970). https://doi.org/10.1016/0022-5193(70)90109-8

[18] Hounsfield, G. N. Patent: Method of and apparatus for examining a body by radiation such as X or gamma radiation, (1969).

[19] Wang, Y., Acoustic emission source localization based on iterative reconstruction algorithm, *Sensors*, **16**, 1174, (2016).

[20] Zhu, W. F., Zhang, H.-Y., Liu, F.-J. et al. Lamb waves topological imaging of multiple blind defects in an isotropic plate, *International Journal of Acoustics and Vibration*, **24**, 320–326, (2019). https://doi.org/10.20855/ijav.2019.24.21479

[21] Andersen, A. H. and Kak, A. C. Simultaneous algebraic reconstruction technique (SART): a superior implementation of the ART algorithm, *Ultrasonic Imaging*, **6**, (1984). https://doi.org/10.1177/016173468400600107

[22] Press, W. H., Teukolsky, S. A., Vetterling, W. T. and Flannery, B. P. *Numerical recipes: the art of scientific computing*, Cambridge University Press, (2007).

[23] Rahman, M. A., Khan, T. I. and Hasan, T, Enhanced damage detection through frequency variation in acoustic emission tomography using the algebraic reconstruction technique, in *31st International Congress on Sound and Vibration*, Incheon, Korea, (2025).

[24] Hassan, M., Khan, T. I., Hasemura, Y. and Islam, M. Performance investigation of two AE source location techniques on a planar multilayer structure, *International Journal of Acoustics and Vibration*, **25**, 226–235, (2020). https://doi.org/10.20855/ijav.2020.25.21635